

First survey of HCNH⁺ in high-mass star-forming cloud cores

F. Fontani^{1,2}, L. Colzi^{3,1}, E. Redaelli², O. Sipilä², and P. Caselli²

¹ INAF-Osservatorio Astrofisico di Arcetri, Largo E. Fermi 5, 50125 Florence, Italy
e-mail: francesco.fontani@inaf.it

² Centre for Astrochemical Studies, Max-Planck-Institute for Extraterrestrial Physics, Giessenbachstrasse 1, 85748 Garching, Germany

³ Centro de Astrobiología (CSIC-INTA), Ctra. de Ajalvir Km. 4, Torrejón de Ardoz, 28850 Madrid, Spain

Received 25 February 2021 / Accepted 14 May 2021

ABSTRACT

Context. Most stars in the Galaxy, including the Sun, were born in high-mass star-forming regions. It is hence important to study the chemical processes in these regions to better understand the chemical heritage of the Solar System and most of the stellar systems in the Galaxy.

Aims. The molecular ion HCNH⁺ is thought to be a crucial species in ion-neutral astrochemical reactions, but so far it has been detected only in a handful of star-forming regions, and hence its chemistry is poorly known.

Methods. We observed with the IRAM 30 m Telescope 26 high-mass star-forming cores in different evolutionary stages in the $J = 3-2$ rotational transition of HCNH⁺.

Results. We report the detection of HCNH⁺ in 16 out of 26 targets. This represents the largest sample of sources detected in this molecular ion to date. The fractional abundances of HCNH⁺ with respect to H₂, [HCNH⁺], are in the range $0.9-14 \times 10^{-11}$, and the highest values are found towards cold starless cores, for which [HCNH⁺] is of the order of 10^{-10} . The abundance ratios [HCNH⁺]/[HCN] and [HCNH⁺]/[HCO⁺] are both ≤ 0.01 for all objects except for four starless cores, which are well above this threshold. These sources have the lowest gas temperatures and average H₂ volume density values in the sample. Based on this observational difference, we ran two chemical models, ‘cold’ and ‘warm’, which attempt to match the average physical properties of the cold(er) starless cores and the warm(er) targets as closely as possible. The reactions occurring in the latter case are investigated in this work for the first time. Our predictions indicate that in the warm model HCNH⁺ is mainly produced by reactions with HCN and HCO⁺, while in the cold model the main progenitor species of HCNH⁺ are HCN⁺ and HNC⁺.

Conclusions. The observational results indicate, and the model predictions confirm, that the chemistry of HCNH⁺ is different in cold-early and warm-evolved cores, and the abundance ratios [HCNH⁺]/[HCN] and [HCNH⁺]/[HCO⁺] can be useful astrochemical tools to discriminate between different evolutionary phases in the process of star formation.

Key words. ISM: molecules – stars: formation – radio lines: ISM – ISM: clouds

1. Introduction

It is now clear that the Sun and most stars in the Milky Way are born in rich clusters that include or are close to high-mass stars (e.g. Carpenter 2000; Pudritz 2002; Adams 2010; Rivilla et al. 2014; Lichtenberg et al. 2019). Therefore, the study of the chemical content and evolution of high-mass star-forming regions can give us important information about the chemical heritage of the Solar System and of most stars in the Milky Way. Despite the importance of studying the chemistry of high-mass star-forming cloud cores (i.e. compact structures with mass $\sim 10-100 M_{\odot}$ that have the potential to form single high-mass stars and/or clusters), an evolutionary classification is not yet clear, due to both observational and theoretical problems (e.g. Beuther et al. 2007; Tan et al. 2014; Motte et al. 2018; Padoan et al. 2020).

Several attempts to empirically give an evolutionary classification of high-mass star-forming cores have been proposed, which can all be tentatively summarised in three coarse phases: (1) high-mass starless cores (HMSCs), which are dense infrared-dark cores characterised by low temperatures ($\sim 10-20$ K) and high densities ($n \geq 10^4-10^5$ cm⁻³), and without clear signs of ongoing star formation like strong protostellar outflows and masers; (2) high-mass protostellar objects (HMPOs),

which are collapsing cores with evidence of one (or more) deeply embedded protostar(s), typically characterised by higher densities and temperatures ($n \approx 10^6$ cm⁻³, $T \geq 20$ K); (3) ultra-compact HII regions (UCHIIs), which are zero age main sequence stars associated with an expanding HII region whose surrounding molecular cocoon ($n \geq 10^5$ cm⁻³, $T \sim 20-100$ K) is affected physically and chemically by its progressive expansion.

Regardless of the evolutionary stage, high-mass star-forming cores are characterised by a complex and rich chemistry (e.g. Fontani et al. 2007; Bisschop et al. 2007; Foster et al. 2011; Belloche et al. 2013; Vasyunina et al. 2014; Coletta et al. 2020). The new generation telescopes have provided a growing amount of observational results including, thanks to their high sensitivity, the detection of rare species (i.e. species with fractional abundance with respect to H₂ lower than $\sim 10^{-10}$). These species can have important implications not only for our understanding of the still mysterious process of high-mass star formation, but also for the chemistry that the primordial Solar System might have inherited from its birth environment (e.g. Beltrán et al. 2009; Fontani et al. 2017; Ligterink et al. 2020; Rivilla et al. 2020; Mininni et al. 2020). Among these rare species, protonated hydrogen cyanide, HCNH⁺ (or iminomethylum), is important in astrochemistry because it is thought to be the main

Table 1. Line parameters obtained from Gaussian fits (Cols. 2–6), and total column densities (beam averaged) of HCNH⁺ obtained from the spectra of the $J = 3-2$ line (Fig. 1), as explained in Sect. 3.

Source	$\int T_{\text{MB}} dV$ K km s ⁻¹	V_p km s ⁻¹	$FWHM$ km s ⁻¹	T_{MB}^p K	1σ K	$T_{\text{ex}}^{(a)}$ K	$N_{\text{tot}}(\text{HCNH}^+)$ $\times 10^{13}$ cm ⁻²	$[\text{HCNH}^+]^{(b)}$ $\times 10^{-11}$
HMSCs								
I00117-MM2	≤0.08	–	2.5 ^(c)	≤0.03	0.01	14	≤0.94	– ^(d)
AFGL5142-EC ^(e)	0.10(0.03)	–2.8(0.3)	2.3(0.8)	0.041	0.014	25	1.0(0.5)	1.4(1.0)
05358-mm3 ^(e)	0.11(0.02)	–16.1(0.3)	3.0(0.7)	0.035	0.01	30	1.2(0.5)	1.7(1.0)
G034-G2	0.21(0.03)	42.9(0.3)	4.3(0.6)	0.05	0.013	16	2.3(0.8)	8.6(4.9)
G034-F2	0.12(0.02)	58.0(0.2)	2.5(0.7)	0.045	0.013	16	1.3(0.5)	12(8)
G034-F1	0.10(0.02)	57.0(0.3)	2.5(0.7)	0.037	0.012	16	1.1(0.5)	14(9)
G028-C1	0.27(0.02)	79.5(0.7)	1.7(0.2)	0.150	0.015	17	2.8(0.8)	12(6)
I20293-WC ^(f)	0.05(0.01)	7.2(0.2)	1.4(0.4)	0.03	0.011	17	0.5(0.2)	1.0(0.7)
I22134-G ^(e)	≤0.06	–	2.5 ^(c)	≤0.024	0.008	25	≤0.61	≤2.6
I22134-B	≤0.07	–	2.5 ^(c)	≤0.03	0.01	17	≤0.74	≤5.7
HMPOs								
00117-MM1	≤0.07	–	1.6 ^(c)	≤0.039	0.013	20	≤0.67	– ^(d)
AFGL5142-MM	0.09(0.02)	–2.3(0.2)	1.9(0.5)	0.045	0.013	34	1.0(0.4)	1.5(1.0)
05358-mm1	0.09(0.02)	–16.1(0.2)	1.4(0.4)	0.06	0.018	39	1.0(0.5)	1.9(1.3)
18 089-1732	0.18(0.07)	32.5(0.3)	2.3(0.6)	0.07	0.020	38	2(1)	3.2(2.6)
18 517+0437	≤0.06	–	1.6 ^(c)	≤0.033	0.011	40	≤0.69	≤1.3
G75-core	≤0.07	–	1.6 ^(c)	≤0.042	0.014	96	≤1.48	≤5.2
I20293-MM1	0.09(0.02)	5.6(0.1)	1.5(0.2)	0.058	0.013	36	1.0(0.4)	3.2(2.0)
I21307	≤0.03	–	1.6(0.3)	≤0.025	0.009	21	≤0.30	≤1.5
I23385	≤0.07	–	1.6 ^(c)	≤0.039	0.013	37	≤0.77	≤4.9
UCHIIs								
G5.89-0.39	0.97(0.04)	8.1(0.6)	2.5(0.1)	0.368	0.024	32	10(3)	2.9(1.5)
I19035-VLA1	≤0.11	–	2.4 ^(c)	≤0.042	0.014	39	1.3(0.3)	5.4(2.4)
19 410+2336	0.08(0.01)	22.5(0.1)	1.4(0.3)	0.054	0.010	21	0.8(0.3)	0.9(0.5)
ON1	0.22(0.2)	11.2(0.1)	3.2(0.3)	0.065	0.010	26	2.2(0.6)	– ^(d)
I22134-VLA1	0.08(0.01)	–18.0(0.1)	1.8(0.3)	0.042	0.009	47	1.0(0.4)	7.3(4.4)
23 033+5951 ^(f)	0.10(0.02)	–53.4(0.4)	3.1(1)	0.031	0.011	25	1.0(0.5)	2.0(1.4)
NGC7538-IRS9	≤0.08	–	2.4 ^(c)	≤0.033	0.011	32	≤0.09	≤1.1

Notes. ^(a)The assumed excitation temperatures are the kinetic temperatures listed in Fontani et al. (2011), and are the same used in Colzi et al. (2018a) to derive the column densities of the HCN isotopologues; ^(b)the HCNH⁺ abundances relative to H₂, [HCNH⁺], are computed from the H₂ column densities given in Fontani et al. (2018), who used averaged values within an area of angular dimension 28'', and thus the given [HCNH⁺] are also average values within 28''; ^(c)fixed FWHM assumed to compute the upper limit on $N_{\text{tot}}(\text{HCNH}^+)$, obtained as the average value of the detected lines in the corresponding evolutionary group; ^(d)column density of H₂ not available; ^(e)warm HMSCs. The other HMSCs are classified as cold (or quiescent; see Fontani et al. 2011). ^(f)tentative detections.

precursor of HCN and HNC. They are both among the most abundant species in star-forming regions, and are believed to have a high pre-biotic potential (Todd & Öberg 2020). Despite its importance, and after the first discovery towards SgrB2 (Ziurys & Turner 1986), HCNH⁺ has been detected in a handful of other star-forming regions: the TMC-1 dark cloud, the DR21(OH) HII region (Schilke et al. 1991), and the low-mass pre-stellar core L1544 (Quénard et al. 2017).

In this work we report 16 new detections of HCNH⁺ towards 26 high-mass star-forming cores almost equally divided into HMSCs, HMPOs, and UCHIIIs. In Sect. 2 we describe the sample and the observational dataset; in Sect. 3 we present the observational results, which we discuss in Sect. 4; in Sect. 5 we describe the chemical model we used to interpret the observational results; and in Sect. 6 we summarise our main findings.

2. Sample and observations

The 26 targets we observed are listed in Table 1. They were taken from the sample presented first by Fontani et al. (2011) and divided into the three gross evolutionary categories discussed in Sect. 1: 10 HMSCs, 9 HMPOs, and 7 UC HIIIs (see Fontani et al. 2011 for details on the source selection criteria). The spectra analysed in this work are part of the dataset published in Fontani et al. (2015a) obtained with the IRAM 30m telescope. In particular, the analysed transition, HCNH⁺ $J = 3-2$, was detected in the band at 1.2 mm of that dataset covering frequencies in the range 216.0–223.78 GHz. The spectra were observed with a telescope beam of ~11'', and a spectral resolution of ~0.26 km s⁻¹. Details of the observations (weather conditions, observing technique, calibration, pointing, and focus checks) are given in Fontani et al. (2015a). The analysed line

has a rest frequency of $\sim 222\,329.277$ MHz, energy of the upper level $E_u \sim 21.3$ K, Einstein coefficient $A_{ij} = 4.61 \times 10^{-6} \text{ s}^{-1}$, and degeneracy of the rotational upper level $g_u = 7$. All these spectral parameters are from the Cologne Database for Molecular Spectroscopy (CDMS; Endres et al. 2016). The spectroscopy was determined by Araki et al. (1998); the dipole moment is from Botschwina (1986). According to the collisional coefficients given in Nkem et al. (2014), which are $\sim 1\text{--}1.5 \times 10^{-10} \text{ s}^{-1}$ in the temperature range 10–100 K, the critical density of the transition is $\sim 4 \times 10^4 \text{ cm}^{-3}$. The lines were fitted with the CLASS package of the GILDAS¹ software using standard procedures.

3. Results

3.1. Detection rate and line shapes

We detected HCNH⁺ $J = 3\text{--}2$ with a signal-to-noise ratio (S/N) higher than ~ 3 towards 14 out of the 26 targets. In two cases, I20293–WC and 23 033+5951, the peak main beam temperature is slightly below the 3σ rms, but the line profile suggests a real line at the limit of the detection level. Hence, we consider them as tentative detections, which provides a total of 16 detected sources including the tentative ones (detection rate $\sim 62\%$). The transition has hyperfine structure, however, that cannot be resolved in our spectra because the separation in velocity of the components is smaller than the velocity resolution. Therefore, we fitted the lines with single Gaussian profiles. This method gives good results with residuals lower than, or comparable to, the noise in the spectra.

Table 1 reports the results of the Gaussian fits to the lines: integrated line intensity ($\int T_{\text{MB}} dV$), velocity at line peak (V_p), line full width at half maximum (FWHM), peak main beam temperature (T_{MB}^p), and 1σ rms in the spectrum (1σ). The uncertainties on V_p and on FWHM are given by the fit procedure. The uncertainties on $\int T_{\text{MB}} dV$ are the sum in quadrature of the error given by the fit and the calibration error on T_{MB} (assumed to be 10%). The latter is dominant in the sum in quadrature.

The spectra and their fits are shown in Fig. 1. In two sources, 18 089–1732 and G5.89–0.39, the line profile cannot be fitted with a single Gaussian. Both spectra show an excess emission in the red tail of the line (see Fig. 1). Towards G5.89–0.39 this excess has the form of a high-velocity wing. Hence, it likely arises from the red-shifted lobe of the outflow associated with the embedded UC HII region (Zapata et al. 2020). Towards 18 089–1732 the excess emission has the shape of a Gaussian peak with intensity almost half of the main peak. Hence, in this case it is more likely due either to a secondary velocity feature or to another line blended with the HCNH⁺ $J = 3\text{--}2$ line. High excitation lines ($E_u \sim 200$ K) of CH₃OCH₃ detected in this source (Coletta et al. 2020) are predicted at $\sim 222\,326$ MHz, which could hence contribute to the secondary peak centred approximately at $\sim 222\,327$ MHz. Moreover, the profile of the H¹³CO⁺ $J = 1\text{--}0$ does not show this secondary peak (Fig. 2), and hence a second velocity feature is very unlikely. A contribution from the red lobe of the outflow associated with the embedded hyper-compact HII region is also possible (Beuther et al. 2010), but because it is not seen in H¹³CO⁺ $J = 1\text{--}0$, its contribution to this secondary peak should be negligible. In general the lack of high-velocity wings, except maybe in the two cases discussed above, indicates that the emission of the line does not arise from shocks and/or outflows, but likely from more quiescent material.

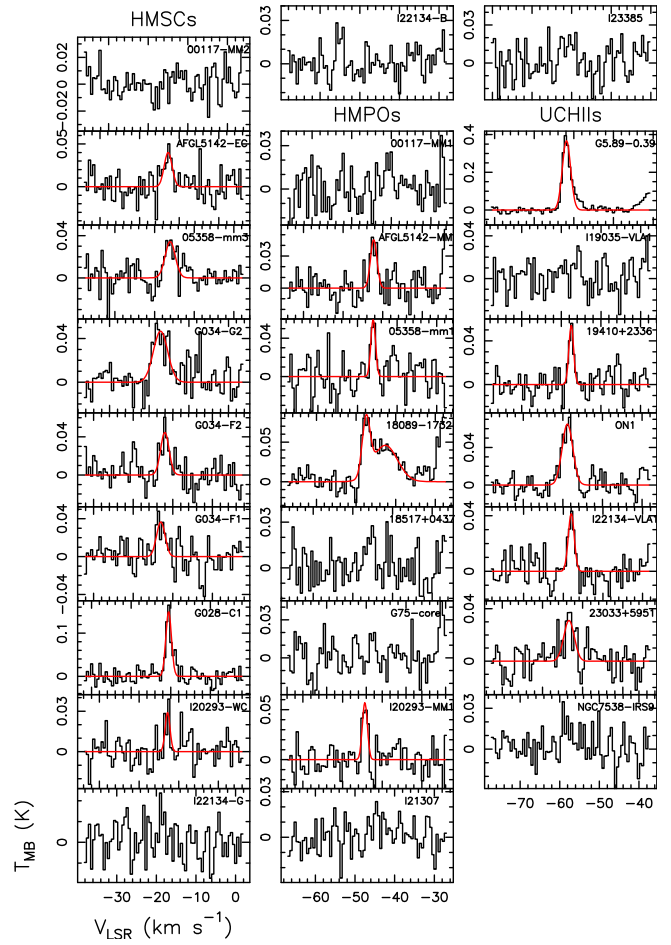


Fig. 1. Observed spectra of HCNH⁺ $J = 3\text{--}2$ obtained with the IRAM 30 m telescope. For each spectrum the velocity interval shown on the x-axis is $\pm 20 \text{ km s}^{-1}$ around the systemic velocity listed in Table A.1 of Fontani et al. (2011). The red curves represent Gaussian fits to the detected lines. For 18 089–1732 a two-Gaussian fit was performed.

Because HCNH⁺ was detected in a handful of star-forming regions before this study, it is not yet clear what kind of material (i.e. with what physical and kinematical properties) is responsible for the emission of this molecule. To investigate this, in Fig. 2 we compare the profiles of HCNH⁺ $J = 3\text{--}2$ with those of H¹³CO⁺ $J = 1\text{--}0$ analysed in Fontani et al. (2018), thought to be a good tracer of the envelope of star-forming cores. Inspection of the plot suggests that in some sources (e.g. G028–C1, AFGL5142–EC, 05358–mm1, I20293–MM1, 19 410+2336) the two lines have similar peak velocity, suggesting a common origin in the envelope of the cores. On the other hand, in some targets (e.g. G034–F1, I20293–WC, I22134–VLA1, and G5.89–0.39) the HCNH⁺ emission does not coincide with the central velocity of H¹³CO⁺, even though towards G034–F1 and I20293–WC, the H¹³CO⁺ $J = 1\text{--}0$ shows multiple velocity features, and the HCNH⁺ $J = 3\text{--}2$ emission is centred on one of these. These second velocity features, in principle, could also be originated by self-absorption or polluting lines from other species. These scenarios, however, are both unlikely in G034–F1 and I20293–WC, because self-absorption signatures were never observed in other lines towards these sources, and polluting lines are very unlikely in cold HMSCs (like these two targets). Furthermore, a second velocity feature towards G034–F1 was found in the HCN isotopologues by Colzi et al. (2018a).

¹ <https://www.iram.fr/IRAMFR/GILDAS/>

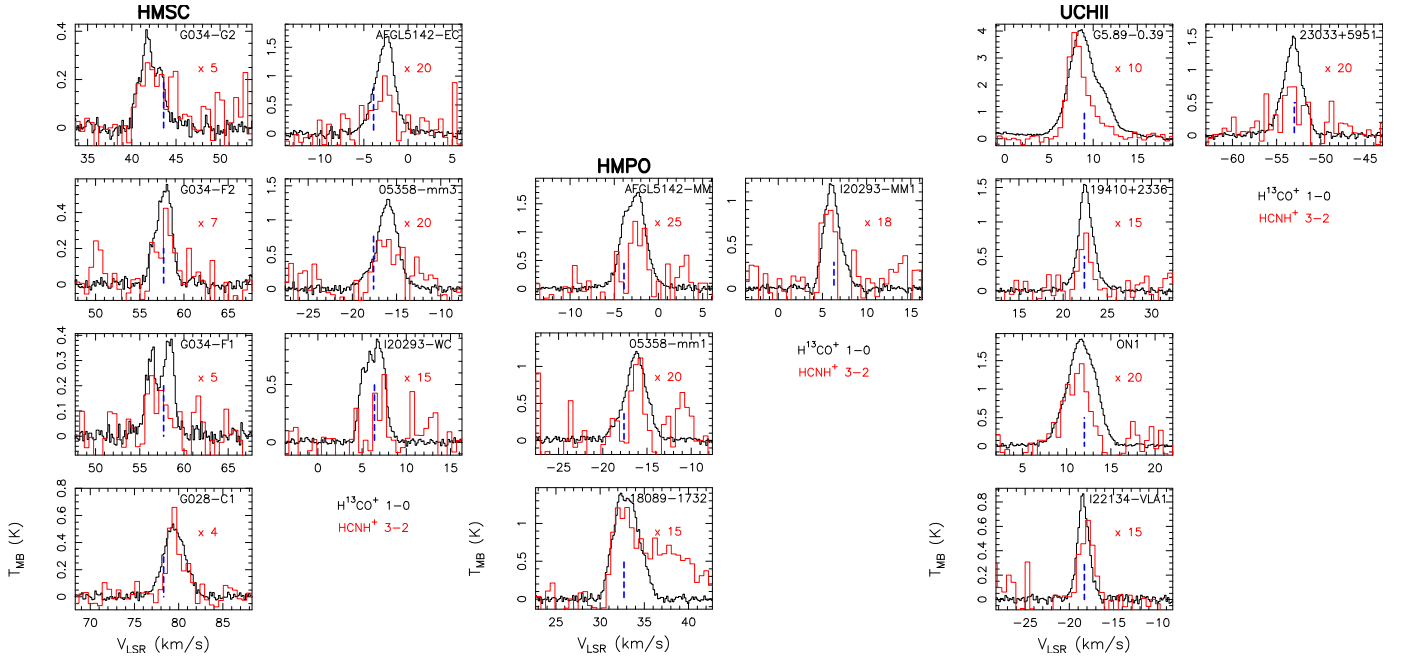


Fig. 2. Comparison among the observed profiles of $\text{H}^{13}\text{CO}^+ J=1-0$ (black histograms) and $\text{HCNH}^+ J=3-2$ (red histograms) towards, *from left to right*, the HMSCs, the HMPOs, and the UCHII detected in HCNH^+ (Table 1). The red number in each plot indicates the multiplicative factor applied to the HCNH^+ spectrum. The blue dashed vertical line indicates the systemic velocity used to centre the observed spectra (see e.g. Fontani et al. 2015a). The peak velocities of HCNH^+ are listed in Table 1.

The stronger H^{13}CO^+ lines generally have broader line widths than the HCNH^+ lines, except for a few targets (G034–G2, 18 089–1732, I22134–VLA1). In addition, we see no hints of high-velocity wings in $\text{HCNH}^+ J=3-2$, except for the already discussed spectrum of G5.89–0.39. However, high-velocity wings could not be detected due to the limited S/N in the spectra. All this indicates that the gas emitting HCNH^+ is mostly quiescent, or not clearly associated with shocks, and that there is not a general agreement with the profiles of the $\text{H}^{13}\text{CO}^+ J=1-0$ lines. We propose, in the targets where both lines have the same velocity peak, that the $\text{HCNH}^+ J=3-2$ line arises from the envelope of the cores, but likely from a more compact portion than that traced by $\text{H}^{13}\text{CO}^+ J=1-0$, because the $\text{HCNH}^+ J=3-2$ line has a higher energy of the upper level than $\text{H}^{13}\text{CO}^+ J=1-0$ (21.3 K versus 4 K), and the spectra were observed with different beam sizes ($\sim 11''$ versus $\sim 28''$).

3.2. Total column densities and abundances of HCNH^+

Assuming that the lines are optically thin and in Local Thermodynamic Equilibrium (LTE), from $\int T_{\text{MB}} dV$, we computed the beam-averaged total column densities of HCNH^+ , $N_{\text{tot}}(\text{HCNH}^+)$, using Eq. (1) of Fontani et al. (2018). For undetected sources, we estimated the upper limits on $N_{\text{tot}}(\text{HCNH}^+)$ from the upper limit on the integrated intensity. This was computed from the relation $\int T_{\text{MB}} dV = 3\sigma \frac{\sqrt{\pi}}{2\sqrt{\ln 2}} FWHM$, which expresses the integral in velocity of a Gaussian line with peak intensity given by the 3σ rms in the spectrum. We assumed as FWHM the average value obtained from the detected lines in each evolutionary group which the undetected source belongs to: 2.5 km s^{-1} for HMSCs, 1.6 km s^{-1} for HMPOs, and 2.4 km s^{-1} for UCHII (see Table 1).

The assumption of optically thin emission is consistent with the low abundance of the molecule and with the fact that the

observed line shapes generally have no hints of high optical depths, such as asymmetric or flat-top profiles. Only towards G034–G2 could the almost flat-top line shape indicate non-negligible optical depths. Hence, in this source the HCNH^+ total column density should be regarded as a lower limit. The assumption of LTE is also reasonable because the critical density of the line ($\sim 4 \times 10^4 \text{ cm}^{-3}$; see Sect. 2) is smaller than, or comparable to, the average H_2 volume densities of the sources. These values, calculated within a beam of $28''$, are between 10^4 and 10^6 cm^{-3} (see e.g. Fontani et al. 2018 and Sect. 4). A few sources have H_2 volume density values of $\sim 1-2 \times 10^4 \text{ cm}^{-3}$: the HMSCs G034–F2, G034–F1, and G028–C1, and the UCHII I22134–VLA1 (see Sect. 4). For these targets, the approximation might not be valid. We estimated by how much $N_{\text{tot}}(\text{HCNH}^+)$ would change in the conservative case where the excitation temperature is lower than the kinetic temperature by 10 K: $N_{\text{tot}}(\text{HCNH}^+)$ would increase by a factor ~ 4 . Therefore, in the following the column densities of these targets should be considered lower limits.

The total column densities, averaged within the telescope beam of $11''$, are in the range $0.5-10 \times 10^{13} \text{ cm}^{-2}$. If we analyse the three evolutionary groups separately, we find hints of possible differences. The average values are $\sim 1.5 \times 10^{13} \text{ cm}^{-2}$ for the HMSCs, $\sim 1.25 \times 10^{13} \text{ cm}^{-2}$ for the HMPOs, and $\sim 2.7 \times 10^{13} \text{ cm}^{-2}$ for the UCHII. However, the average value in the UCHII is strongly biased by G5.89–0.39, which is by far the most luminous object in the sample. Without G5.89–0.39 the average value in the UCHII is $\sim 1.3 \times 10^{13} \text{ cm}^{-2}$, consistent with those of the other two evolutionary groups.

We computed abundances of HCNH^+ relative to H_2 by using the H_2 column densities published in Fontani et al. (2018). These were average values derived in an angular diameter of $28''$, hence the HCNH^+ column densities were smoothed to this larger angular diameter. The corresponding abundances, $[\text{HCNH}^+]$, are listed in Table 1, and range from ~ 0.9 to $\sim 14 \times 10^{-11}$. Interestingly, HMPOs and UCHII have average $[\text{HCNH}^+]$ of the order

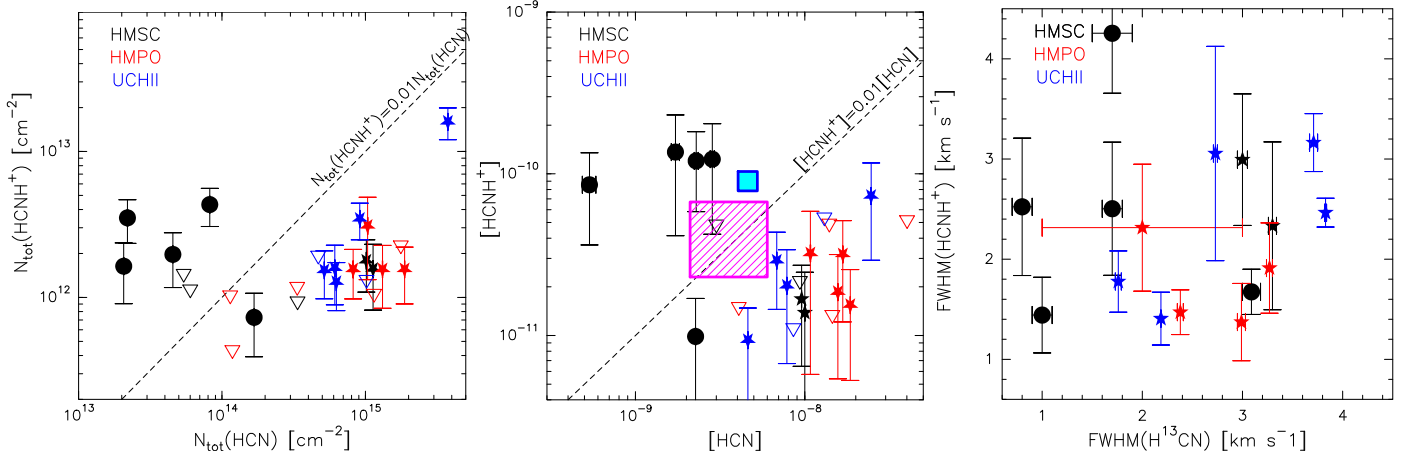


Fig. 3. *Left panel:* comparison between $N_{\text{tot}}(\text{HCNH}^+)$ and $N_{\text{tot}}(\text{HCN})$. The latter was derived from the $\text{H}^{13}\text{CN } J=1-0$ line (Colzi et al. 2018b), assuming the same T_{ex} , by correcting it for the $^{12}\text{C}/^{13}\text{C}$ ratio obtained at the Galactocentric distance of the sources from the trend of Yan et al. (2019). $N_{\text{tot}}(\text{HCNH}^+)$ has been rescaled to the (larger) beam of the H^{13}CN observations, $\sim 28''$. Red stars are HMPOs; blue stars are UCHIIs; black symbols are HMSCs (filled circles for quiescent, stars for warm; see Table 1). Triangles indicate upper limits on $N_{\text{tot}}(\text{HCNH}^+)$. The dashed line is the locus where $N_{\text{tot}}(\text{HCNH}^+) = 0.01 N_{\text{tot}}(\text{HCN})$. *Middle panel:* same as left panel, but for the fractional abundances with respect to H_2 calculated on a beam of $\sim 28''$. The purple rectangle indicates the range of abundances that reproduces the observed $[\text{HCN}]$, and $[\text{HCNH}^+]$ in the predictions of the WM (see Sect. 5 and right panel of Fig. 7). Similarly, the cyan square indicates the prediction of the CM (see Sect. 5 and left panel of Fig. 7). *Right panel:* comparison between the line FWHM of HCNH^+ , derived in this work from the $J=3-2$ line, and H^{13}CN , derived by Colzi et al. (2018a) from the $J=1-0$ line at ~ 87 GHz. The symbols have the same meaning as those in the left and middle panels.

of 10^{-11} and are consistent with each other (specifically, ~ 2.5 and $\sim 3.7 \times 10^{-11}$, respectively), while HMCSs have an average $[\text{HCNH}^+]$ of $\sim 7.3 \times 10^{-11}$ (i.e. a factor 2–3 higher). In particular, the HMCSs with the highest abundances are all classified as cold or quiescent by Fontani et al. (2011), and have $[\text{HCNH}^+]$ of the order of $\times 10^{-10}$.

4. Discussion of the observational results

One of the most important and direct findings from the parameters in Table 1 is that the HMSCs classified as quiescent have HCNH^+ abundances that are about an order of magnitude higher with respect to warm(er) and/or more evolved objects. This suggests that in cold and quiescent cores some formation pathways of HCNH^+ are more efficient than in warmer cores and/or that some destruction pathways are less efficient. The chemistry of HCNH^+ is thought to be related to that of HCN , HCO^+ , and CN , as discussed in Quénard et al. (2017). However, Quénard et al. (2017) focussed on the pre-stellar core L1544 (i.e. a cold core with a known physical structure). It is not yet clear what the dominant formation pathways are in warmer environments (and under different physical conditions in general).

To investigate the chemical origin of HCNH^+ we searched for correlations between some physical parameters of HCNH^+ and those of HCN , HCO^+ , and CN . In Fig. 3 we compare column densities, abundances, and FWHM of HCNH^+ and HCN . Figure 4 shows the same comparison between HCNH^+ and HCO^+ . We note that the column densities of HCN and HCO^+ were calculated from the data of H^{13}CN and H^{13}CO^+ published in Colzi et al. (2018a) and Fontani et al. (2018), respectively. The column densities of both H^{13}CN and H^{13}CO^+ were computed assuming the T_{ex} in Table 1, and converted to those of the main isotopologues using the $^{12}\text{C}/^{13}\text{C}$ ratio at the Galactocentric distance of the sources. This latter value was derived from the most recent trend of Yan et al. (2019). Calculated $^{12}\text{C}/^{13}\text{C}$ ratios are in the range $\sim 40-70$. The uncertainties on these ratios,

calculated propagating the errors on the parameters of the Galactocentric trend, are of the order of 30%. As for HCNH^+ , the final $N_{\text{tot}}(\text{HCN})$ and $N_{\text{tot}}(\text{HCO}^+)$ were scaled to the same beam of $\sim 28''$, and the abundances $[\text{HCN}]$ and $[\text{HCO}^+]$ were computed dividing $N_{\text{tot}}(\text{HCN})$ and $N_{\text{tot}}(\text{HCO}^+)$ by the same $N_{\text{tot}}(\text{H}_2)$ used for HCNH^+ .

Two relevant results emerge clearly from the plots in Figs. 3 and 4: first, the abundance ratios $[\text{HCNH}^+]/[\text{HCN}]$ and $[\text{HCNH}^+]/[\text{HCO}^+]$ are both ≤ 0.01 for all objects except for the four quiescent HMSCs G034–G2, G034–F2, G034–F1, and G028–C1, for which they are one order of magnitude above this threshold. This difference could be even more pronounced for three of these four sources because, as discussed in Sect. 3.2, $[\text{HCNH}^+]$ might be underestimated because the transition could be sub-thermally excited. Second, the FWHM of the lines of the different species do not appear to be clearly correlated. However, if the four quiescent HMSCs mentioned above are excluded, a tentative correlation is apparent in Figs. 3 and 4, with Spearman ρ correlation coefficients ~ 0.55 and ~ 0.63 , respectively.

These findings suggest that the dominant formation pathways of HCNH^+ in cold and warm regions are likely different. Only one quiescent HMSC, I20293–WC, does not follow this different behaviour. However, the detection of HCNH^+ is tentative towards this source (see Table 1), and the core, even though considered quiescent based on its low kinetic temperature (Fontani et al. 2011), is embedded in a star-forming region harbouring a more evolved object (e.g. core I20293–MM1, included in the HMPOs). Therefore, the chemistry in this target could be influenced by the complex environment in which it is embedded.

Figure 5 shows the same comparison of physical parameters as in Figs. 3 and 4 for CN . The properties of this species were derived from ^{13}CN by Fontani et al. (2015b). Figure 5 shows a less clear dichotomy between HMSCs and the more evolved targets, but unfortunately the comparison is affected by the non-detection of ^{13}CN in all the quiescent HMSCs. However, also in this case the $[\text{HCNH}^+]/[\text{CN}]$ ratio in warm and/or evolved

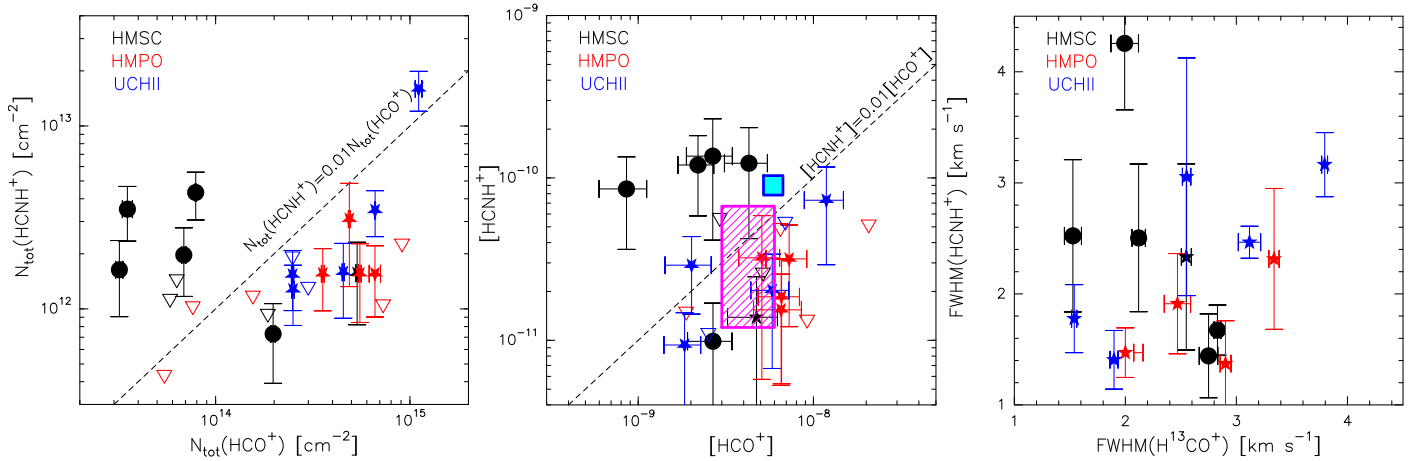


Fig. 4. *Left panel:* comparison between $N_{\text{tot}}(\text{HCNH}^+)$ and $N_{\text{tot}}(\text{HCO}^+)$. The latter was computed from $N_{\text{tot}}(\text{H}^{13}\text{CO}^+)$ taken from [Fontani et al. \(2018\)](#) by correcting it for the $^{12}\text{C}/^{13}\text{C}$ ratio obtained at the Galactocentric distance of the sources from the trend of [Yan et al. \(2019\)](#). *Middle panel:* same as left panel, but for the abundances relative to H_2 . As in the middle panel of [Fig. 3](#), the purple rectangle and the cyan square show the predictions of the WM and CM (Sect. 5 and [Fig. 7](#)), respectively, that best reproduce the observed abundances of the three species HCNH^+ , HCN , and HCO^+ . *Right panel:* comparison between the line FWHM of HCNH^+ , derived in this work from the $J=3-2$ line, and H^{13}CO^+ , derived in [Fontani et al. \(2018\)](#) from the $J=1-0$ line at ~ 87 GHz. The symbols have the same meaning as those in the left and middle panels.

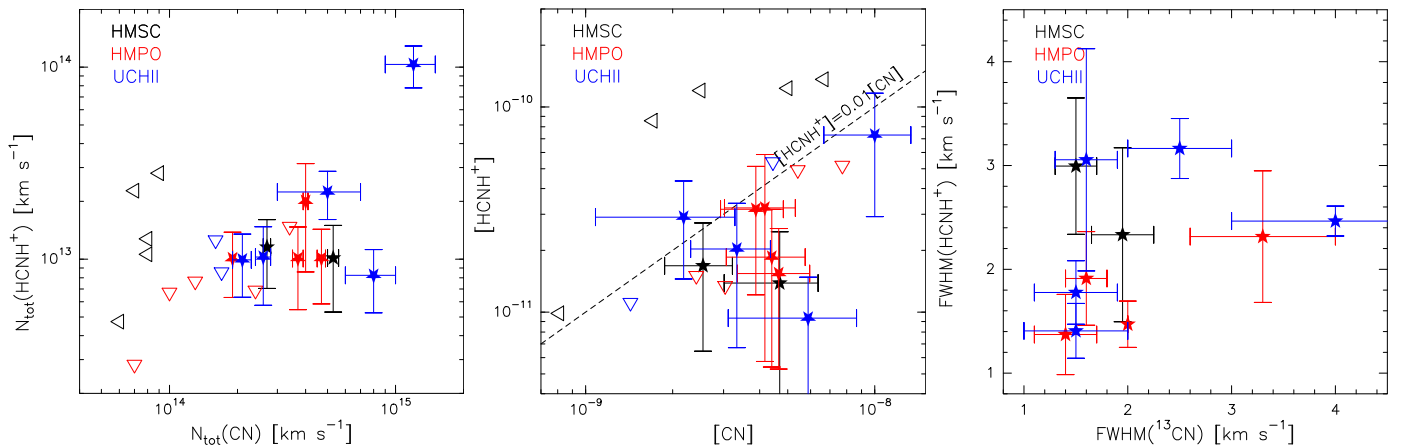


Fig. 5. Same as [Fig. 3](#), but for the comparison between HCNH^+ and CN . For CN , N_{tot} (*left panel*), $[\text{CN}]$ (*middle panel*), and FWHM (*right panel*) are derived from observations of the $^{13}\text{CN } N=2-1$ line at ~ 217 GHz, published in [Fontani et al. \(2015b\)](#). $N_{\text{tot}}(\text{HCNH}^+)$ and $N_{\text{tot}}(\text{CN})$ are averaged within the same beam of $\sim 11''$, and left-pointing triangles are upper limits on $N_{\text{tot}}(\text{CN})$, while down-pointing triangles are upper limits on $N_{\text{tot}}(\text{HCNH}^+)$. $[\text{HCNH}^+]$ and $[\text{CN}]$ are averaged within a beam of $28''$.

objects is ≤ 0.01 . The FWHM of the lines does not seem correlated either, and hence the possible chemical relation between HCNH^+ and CN seems unlikely.

Finally, in [Fig. 6](#) we plot the column density ratio $N_{\text{tot}}(\text{HCNH}^+)/N_{\text{tot}}(\text{HCN})$ as a function of the following core physical parameters: $N_{\text{tot}}(\text{HCN})$; volume density of H_2 , $n(\text{H}_2)$; gas kinetic temperature, T_k , taken from [Fontani et al. \(2011\)](#) and used in [Colzi et al. \(2018a\)](#) to compute the HCN column densities; dust temperature, T_{dust} , calculated by [Mininni et al. \(2021\)](#) from grey-body fits to the spectral energy distribution of the sources derived from the *Herschel* bands. $n(\text{H}_2)$ is an average value within $28''$ computed from the column density of H_2 given in [Fontani et al. \(2018\)](#) assuming spherical sources for simplicity. Based on this plot, the different behaviour of cold and warm sources is very clear: colder and less dense objects have $N_{\text{tot}}(\text{HCNH}^+)/N_{\text{tot}}(\text{HCN})$ ratios that are about an order of magnitude higher than warmer and denser ones.

5. Chemical modelling

In this section we investigate the main routes of formation and destruction of HCNH^+ and HCN , together with the possible chemical relation with HCO^+ , for two different chemical models that represent the colder and warmer conditions of the sample of high-mass star-forming regions studied in this work.

5.1. Description of the models

For the chemical simulations we use our gas-grain chemical code, recently described in [Sipilä et al. \(2019a,b\)](#). The chemical networks used here contain deuterium and spin-state chemistry (see [Sipilä et al. 2019b](#), and references therein). While we do not explicitly consider deuterium chemistry in this paper, the inclusion of spin-state chemistry is important due to its effect on nitrogen chemistry (e.g. [Dislaire et al. 2012](#)). The chemical network contains a combined total of 881 species and

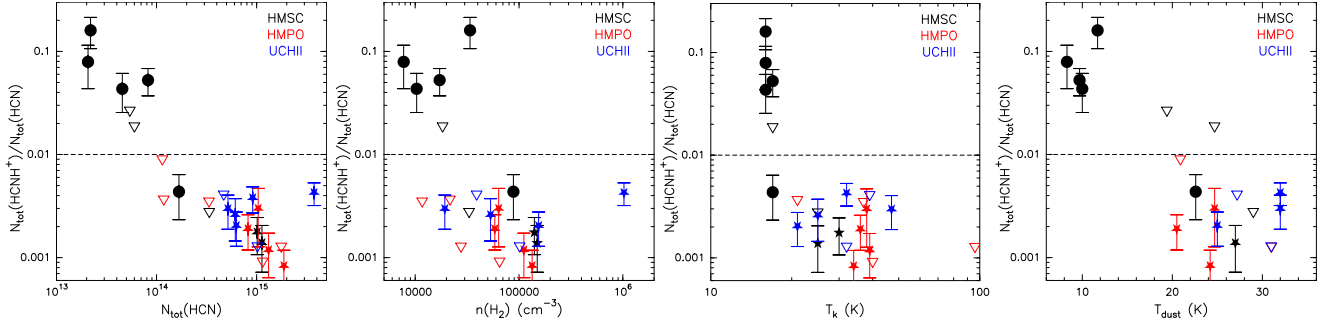


Fig. 6. Comparison between the column density ratio $N_{\text{tot}}(\text{HCNH}^+)/N_{\text{tot}}(\text{HCN})$ and the following physical parameters of the cores (from left to right): $N_{\text{tot}}(\text{HCN})$, $n(\text{H}_2)$, T_{k} , and T_{dust} . The dashed line in each plot indicates $N_{\text{tot}}(\text{HCNH}^+)/N_{\text{tot}}(\text{HCN}) = 0.01$.

Table 2. Initial abundances with respect to n_{H} (adapted from Semenov et al. 2010).

Species	Initial abundance
H ₂	0.5
He	9.00×10^{-2}
C ⁺	1.20×10^{-4}
N	7.60×10^{-5}
O	2.56×10^{-4}
S ⁺	8.00×10^{-8}
Si ⁺	8.00×10^{-9}
Na ⁺	2.00×10^{-9}
Mg ⁺	7.00×10^{-9}
Fe ⁺	3.00×10^{-9}
P ⁺	2.00×10^{-10}
Cl ⁺	1.00×10^{-9}
F	2.00×10^{-9}
ortho-para (o/p)	10^{-3}

40 515 reactions (37 993 gas-phase reactions and 2519 grain-surface reactions). We have excluded all molecules that contain more than five atoms so that the chemical simulations can run faster; this is justified in the present context where we study the chemistry of molecules with four atoms or fewer. The initial abundances adopted in the models are summarised in Table 2.

To discuss the results obtained from the observations we decided to model two types of molecular clouds defined dividing the sample of sources into two sub-groups:

- cold model (CM): defined from the four sources with a T_{dust} of about 10 K (see right panel of Fig. 6). These sources are the HMSCs G034–G2, G034–F1, G034–F2, and G028–C1;
- warm model (WM): defined from all of the other sources, which have $T_{\text{dust}} > 10$ K.

We fixed the cosmic-ray ionisation rate (ζ), the visual extinction (A_{V}), the grain albedo (ω), the grain radius (a_{g}), the grain material density (ρ_{g}), the ratio of the diffusion to the binding energy of a species on dust grains (ϵ), and the dust-to-gas mass ratio (R_{d}) to the values given in Table 3. The gas temperature (T_{gas}) and total number density of H nuclei² (n_{H}) of the two models were defined respectively from the average T_{dust} and $n(\text{H}_2)$ of the two sub-groups of sources. We decided to use the dust temperatures instead of the kinetic temperatures because they were all derived with the same method (Mininni et al. 2021), while the kinetic temperatures were not; we assumed

² $n_{\text{H}} = n(\text{H}) + 2n(\text{H}_2) \approx 2n(\text{H}_2)$ in dense molecular clouds like those simulated in this work.

Table 3. Values of the physical parameters fixed in each model.

Parameter	Value
ζ	$1.3 \times 10^{-17} \text{ s}^{-1}$
A_{V}	10 mag
ω	0.6
a_{g}	10^{-5} cm
ρ_{g}	3 g cm^{-3}
$\epsilon = E_{\text{diff}}/E_{\text{b}}$	0.6
$R_{\text{d}} = \text{dust-to-gas mass ratio}$	0.01
T_{gas}	10 K (CM)
	27 K (WM)
n_{H}	$3.4 \times 10^4 \text{ cm}^{-3}$ (CM)
	$2.4 \times 10^5 \text{ cm}^{-3}$ (WM)

$T_{\text{gas}} = T_{\text{dust}}$ for simplicity. For the cold model $T_{\text{gas}} = 10$ K and $n_{\text{H}} = 3.4 \times 10^4 \text{ cm}^{-3}$, and for the warm model $T_{\text{gas}} = 27$ K and $n_{\text{H}} = 2.4 \times 10^5 \text{ cm}^{-3}$. We adopted as initial conditions those used by Colzi et al. (2020) with an ortho-para ratio (o/p) of 10^{-3} . Since in warm regions (> 20 K) the o/p could be higher, and because N chemistry may be affected by it, we tried also to assume an o/p for the WM of 10^{-2} and of 10^{-1} . This test was done with a fixed temperature of 27 K and we do not take into account the possibility that the o/p could be even higher while the temperature increases. In both cases the results that are discussed in the next section do not change.

It should be noted that for this work, both for the observations and for the chemical modelling, we discard any possible effect from the chemical isotopic fractionation of carbon, which could modify the observed and modelled abundances of HCN and HCO⁺ at most by a factor of three (see Colzi et al. 2020). Gas-grain chemistry is followed in our chemical models, and is important in the differentiation between the warm and cold sources, as in the former CO can be mainly maintained in the gas phase (27 K is just above the sublimation temperature of CO), thus contributing to the higher HCO⁺ abundances in warm regions.

5.2. Model predictions

Figure 7 shows the predicted abundances for HCNH⁺, HCN, and HCO⁺. These predictions are plotted together with the range of the observed abundances, derived as explained in Sect. 3.2. For the CM the three abundances can be partially reproduced at about $t_{\text{CM}} = 4 \times 10^5$ yr. For the WM this happens at two times, 5×10^4 yr and 3×10^6 yr, but for this discussion we decided to take into account only the earlier one ($t_{\text{WM}} = 5 \times 10^4$ yr), which

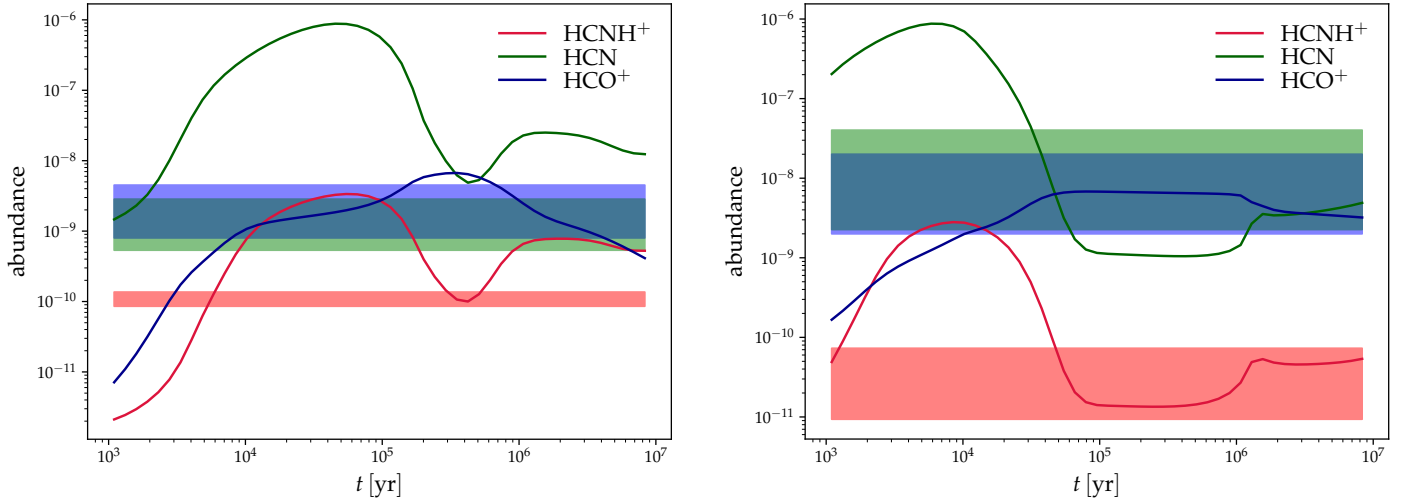


Fig. 7. Time evolution of HCNH⁺, HCN, and HCO⁺ abundances with respect to H₂ for the CM (left panel) and for the WM (right panel). The coloured horizontal bands represent the ranges of observed abundances for HCNH⁺ (red), HCN (green), and HCO⁺ (blue), for the two sub-groups of sources.

is more representative of the life-time of massive star-forming regions (e.g. Motte et al. 2018). Moreover, at these times the abundance of HCN is equal to that of HCO⁺ as it is observed towards the sources studied in this work (see Figs. 3 and 4).

On these timescales most of the HCN and HCNH⁺ are already formed through the early-time chemistry (see e.g. Hily-Blant et al. 2010), HCN being mainly formed from



and HCNH⁺ from



The abundances of both HCN and HCNH⁺ increase by one order of magnitude at chemical times of 10⁴ yr (Fig. 7).

As shown in Fig. 8, the observed HCNH⁺/HCN ratio cannot be reproduced by our chemical models on the timescales for which the abundances are reproduced. The predicted HCNH⁺/HCN ratio at t_{CM} is ~ 0.02 , lower than the observed ratios, and at t_{WM} is ~ 0.01 , slightly higher than what is observed. However, observations and model predictions agree with a higher HCNH⁺/HCN ratio in colder sources with respect to the warmer ones.

5.3. Formation and destruction reactions of HCNH⁺

To perform a detailed analysis and discuss the observed differences between the two sub-groups of sources (i.e. cold early starless cores and warmer evolved objects), we studied in detail the main reactions of formation and destruction that involve HCN, HCNH⁺, and related chemical species. In particular, we took into account the t_{CM} and t_{WM} times. In both models HCO⁺ is formed mainly from CO + H₃⁺ and mainly destroyed by HCO⁺ dissociative recombination. However, as we discuss later, its presence is very important in the cycle of reactions involved in the warm model.

Regarding the cold model, HCNH⁺ is mainly formed via

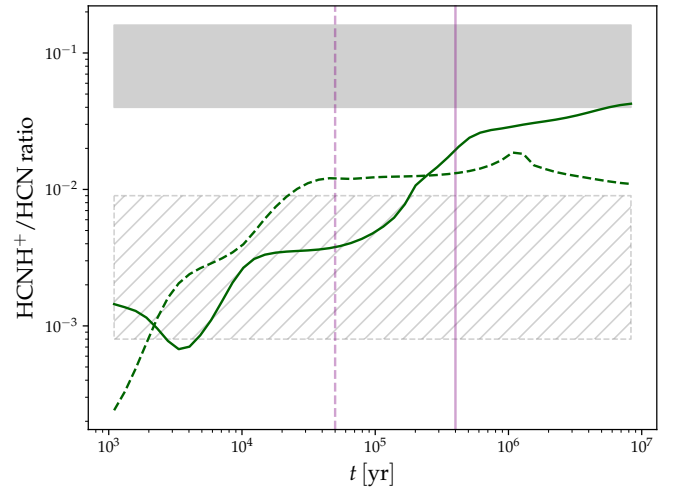
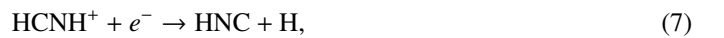


Fig. 8. Predicted HCNH⁺/HCN ratio for the CM (green solid line) and for the WM (dashed green line). The grey shaded areas represent the range of observed HCNH⁺/HCN ratios for the CM (filled area), and for the WM (striped area). The purple vertical lines indicate the times at which the abundances of HCNH⁺, HCN, and HCO⁺ are reproduced by the CM ($t_{\text{CM}} = 4 \times 10^3$ yr, solid line), and by the WM ($t_{\text{WM}} = 5 \times 10^4$ yr, dashed line).

and



and mainly destroyed by dissociative recombination forming HCN, HNC, and CN with almost the same probability (33.5, 33.5, and 33%, respectively; Semaniak et al. 2001):



and



Moreover, HCN⁺ is mainly formed via CN + H₃⁺ closing this part of the cycle of reactions (Woon & Herbst 2009). Another cycle of

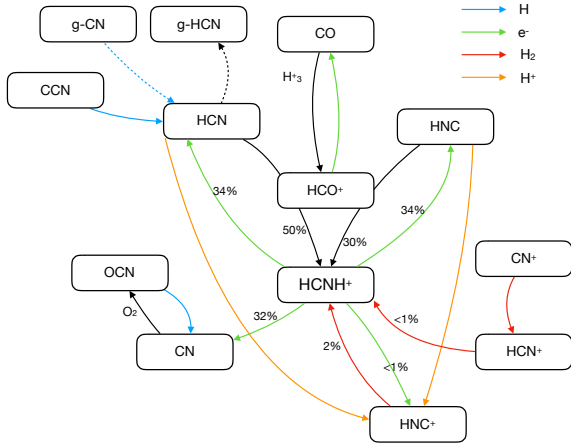
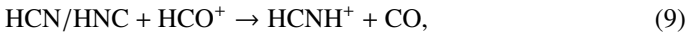


Fig. 9. Scheme of the chemical network that connects the main molecular species investigated in this work for the WM (see Sect. 5.1). The prefix *g-* indicates molecules in icy mantles on dust grains. The arrows are colour-coded depending on the involved reactant: H (blue), H₂ (red), free electrons (green), H⁺ (orange), other species (black; the reactant is indicated on the side). Dashed arrows refer to transitions from solid to gas phase, or vice versa. For the reactions forming and destroying HCNH⁺, their relative contribution (in percentage) is also indicated.

reactions involves HCN, which at t_{CM} is mainly formed via reaction (6) and mainly destroyed by the presence of HCO⁺, C⁺, and H₃⁺. All of this is in agreement with the predictions of Hily-Blant et al. (2010) and Loison et al. (2014) for low-temperature pre-stellar cores and dark molecular clouds, respectively. More recently, for HCNH⁺, this was also confirmed by Quénard et al. (2017) towards the pre-stellar core L1544.

The novelty of this work is the study of the main chemical reactions for these chemical species in an environment that is warmer and denser than in the previous studies. From the WM we find that HCNH⁺ is mainly formed via



instead of reactions (3) and (4). Although these two reactions still occur, they are not efficient any more for the formation of protonated HCN because the abundances of HCN⁺ and HNC⁺ decrease by three orders of magnitude with respect to the CM. The cycle of main reactions for the warm model is shown in Fig. 9. These chemical pathways are in agreement with the tentative correlations found for the FWHM between HCNH⁺ and HCN and HCO⁺.

5.4. Discussion of the assumed parameters

It is worth noting that the sources have very complex structure, with dense cores embedded in a diffuse envelope, and also with the possible presence of extended outflows from the massive protostellar objects. In these models we simplify the physical geometry of the sources, and most of the parameters are assumed to be constant during the chemical evolution, possibly affecting the predicted abundances. Hence, we checked whether changing some of the physical parameters of the two models could lead to a better agreement with the absolute HCNH⁺/HCN ratios observed.

First of all, we tested higher values of the cosmic-ray ionisation rate with respect to the canonical value of $1.3 \times 10^{-17} \text{ s}^{-1}$ (e.g. Padovani et al. 2009), of 10^{-16} , 10^{-15} , and 10^{-14} s^{-1} (e.g. López-Sepulcre et al. 2013; Fontani et al. 2017). We find a higher

HCNH⁺/HCN ratio (up to 0.04 already at 10^5 yr) at the lower edge of the observed values, for higher ζ in the CM (see left panel of Fig. 10). The presence of more ions favours the destruction of HCN over the formation of HCNH⁺. Moreover, this trend is the same for the WM, making the observed values reproduced for lower ζ (see right panel of Fig. 10). However, these trends are hard to understand because the ζ measured towards HMSCs are lower with respect to those found towards protostellar objects (e.g. Fontani et al. 2017). Another discrepancy is that the observed abundances of the molecules could not be reproduced, for both models, at times when the HCNH⁺/HCN ratio matches (see Figs. A.1–A.3). Thus, the cosmic-ray ionisation rate could not help us to explain the observed values.

Secondly, we investigated the possibility of a higher number density of hydrogen nuclei for the CM. In fact, n_{H} were found from the H₂ column densities, which in turn were derived in an area with angular dimension $28''$. However, the emission is not resolved and in principle it could mainly come from a smaller region (dense cores inside the high-mass clump). This would lead to higher n_{H} . Assuming a density of one order of magnitude higher ($n_{\text{H}} = 3.4 \times 10^5 \text{ cm}^{-3}$) we find a better agreement with respect to the observed abundances of HCN, which are lower with respect to the predictions of the initial cold model (Fig. 11). The higher density, together with the low temperature, makes adsorption onto grain surfaces more efficient. However, the abundance of HCNH⁺ also decreases.

Finally, since high-mass protostellar objects are born in a gas that was previously a starless core, we tried to model the warm sources using as initial conditions the abundances of the CM at $4 \times 10^5 \text{ yr}$, the time in which the CM observations are reproduced. Interestingly, we found a warm model with almost constant abundances for the three models, well reproduced by the observations of HCN and HCO⁺, while slightly above with respect to the observed HCNH⁺ (Fig. 12). This leads to the same result obtained in the original WM, but spread during the chemical evolution.

In conclusion, we have found that a change in the initial conditions or in some of the initial parameters of the chemical model would not lead to the absolute observed HCNH⁺/HCN ratios. Many of the relevant reactions in the chemical model are not well constrained, and perhaps some important pathways are missing. For example, reactions (3), (4), and (9) in the KInetic Database for Astrochemistry (KIDA) network are just estimated and laboratory measurements are needed to obtain the correct molecular abundances.

6. Summary and conclusions

We have presented the first survey of HCNH⁺ $J=3-2$ lines, observed with the IRAM 30 m telescope, towards 26 high-mass star-forming regions. We report 14 detections and 2 tentative detections, for a total detection rate of $\sim 62\%$. The total column densities, $N_{\text{tot}}(\text{HCNH}^+)$, calculated assuming optically thin lines and local thermodynamic equilibrium conditions, are in the range $0.5-10 \times 10^{14} \text{ cm}^{-2}$. The abundances of HCNH⁺ with respect to H₂ are in the range $0.9-14 \times 10^{-11}$, and the highest values are found towards the coldest HMSCs, for which [HCNH⁺] is of the order of 10^{-10} . The abundance ratios [HCNH⁺]/[HCN] and [HCNH⁺]/[HCO⁺] are both ≤ 0.01 in all targets except towards the four coldest HMSCs. Hence, the dominant formation pathways of HCNH⁺ in cold-early and warm-evolved regions are likely different. We have run two chemical models, one cold and one warm, in an attempt to

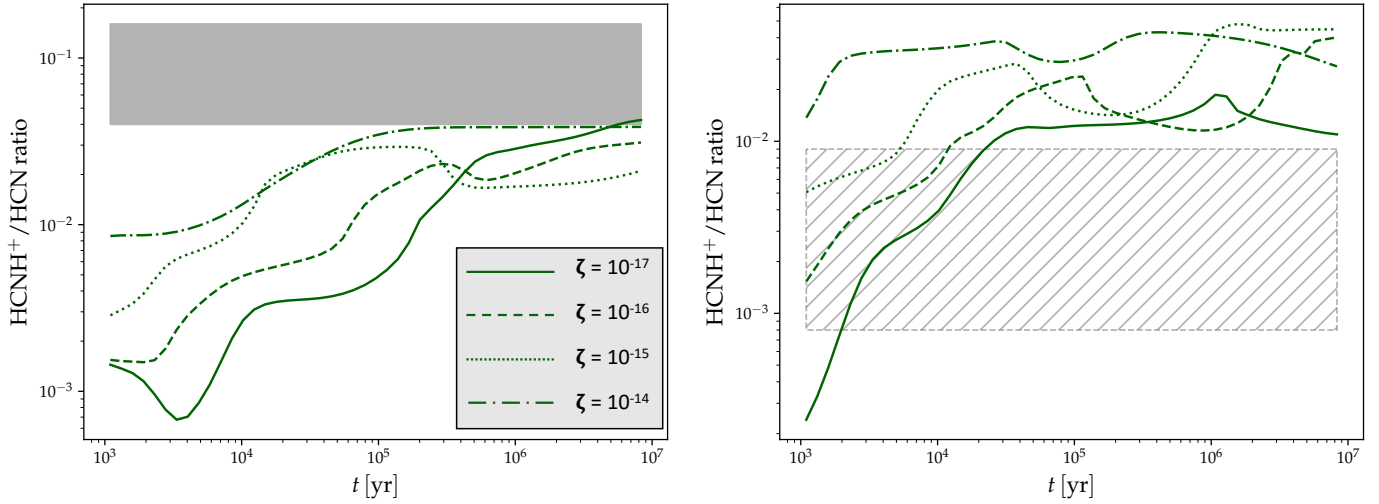


Fig. 10. Predicted HCNH^+/HCN ratio for the CM (left panel) and the WM (right panel), assuming different cosmic-ray ionisation rates, ζ . The grey shaded areas represent the range of observed HCNH^+/HCN ratios for the CM (filled area in the left panel), and for the WM (striped area in the right panel).

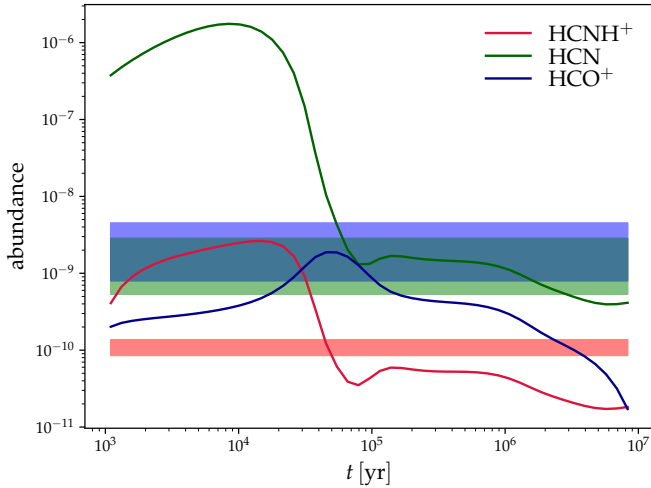


Fig. 11. Time evolution of HCNH^+ , HCN, and HCO^+ abundances with respect to H_2 for the cold model, but assuming a higher n_{H} of $3.4 \times 10^5 \text{ cm}^{-3}$. The coloured horizontal areas are the same as in the left panel of Fig. 7.

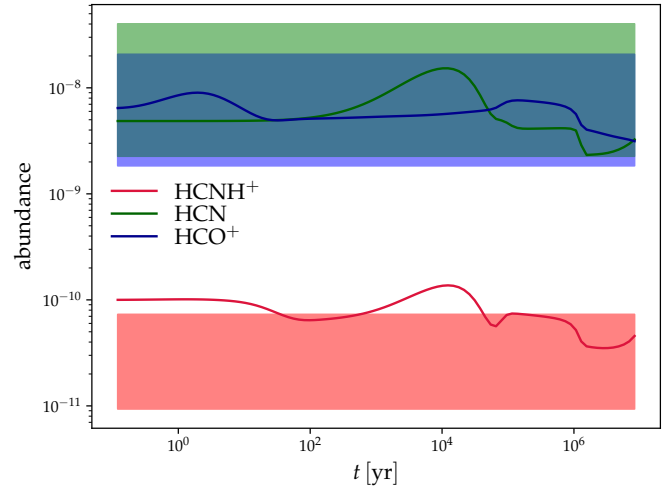


Fig. 12. Time evolution of HCNH^+ , HCN, and HCO^+ abundances with respect to H_2 for the warm model, found assuming as initial conditions the abundances of the CM at t_{CM} . The coloured horizontal areas are the same as the right panel of Fig. 7.

reproduce our results. Besides the different temperatures, the two models are also adapted to match as closely as possible the average physical conditions of the four cold(est) HMSCs and the other sources. In particular, the main chemical reactions leading to the formation and destruction of HCNH^+ in the warm model are investigated in this work for the first time. Our predictions indicate that HCO^+ and HCN/HNC are indeed the dominant progenitor species of HCNH^+ in the warm model, while in the cold model HCNH^+ is mainly formed by HCN^+ and HNC^+ . Another important result of this study is that the abundance ratios $[\text{HCNH}^+]/[\text{HCN}]$ and $[\text{HCNH}^+]/[\text{HCO}^+]$ can be a useful astrochemical tool for discriminating between different evolutionary phases in the process of star formation. Naturally, higher angular resolution observations will allow us to better constrain the precise location and the extent of the emitting region of HCNH^+ in the sources. More transitions will also help in constraining more precisely the excitation conditions, both

crucial elements to better define the range of physical parameters appropriate to model the chemistry.

Acknowledgements. We thank the anonymous referee for their valuable and constructive comments. F.F. is grateful to the IRAM 30m staff for their precious help during the observations. L.C. acknowledges financial support through Spanish grant ESP2017-86582-C4-1-R (MINECO/AEI). L.C. also acknowledges support from the Comunidad de Madrid through the Atracción de Talento Investigador Modalidad 1 (Doctores con experiencia) Grant (COOL: Cosmic Origins Of Life; 2019-T1/TIC-15379; PI: Rivilla). The research leading to these results has received funding from the European Commission Seventh Framework Programme (FP/2007-2013) under grant agreement No 283393 (RadioNet3).

References

- Adams, F. C., 2010, *ARA&A*, 48, 47
 Araki, M., Ozeki, H., & Saito, S. 1998, *ApJ*, 496, L53
 Belloche, A., Müller, H. S. P., Menten, K. M., Schilke, P., & Comito, C. 2013, *A&A*, 559, A47
 Beltrán, M. T., Codella, C., Viti, S., Neri, R., & Cesaroni, R. 2009, *ApJ*, 690, L93

- Beuther, H., Churchwell, E. B., McKee, C. F., & Tan, J. C. 2007, in *Protostars and Planets V* (Tucson: University of Arizona Press), 165
- Beuther, H., Vlemmings, W. H. T., Rao, R., & van der Tak, F. F. S. 2010, *ApJ*, **724**, L113
- Bisschop, S. E., Jørgensen, J. K., van Dishoeck, E. F., & de Wachter, E. B. M. 2007, *A&A*, **465**, 913
- Botschwina, P. 1986, *Chem. Phys. Lett.*, **124**, 382
- Carpenter, J. M. 2000, *AJ*, **120**, 3139
- Coletta, A., Fontani, F., Rivilla, V. M., et al. 2020, *A&A*, **641**, A54
- Colzi, L., Fontani, F., Rivilla, V. M., et al. 2018a, *MNRAS*, **478**, 3693
- Colzi, L., Fontani, F., Caselli, P., et al. 2018b, *A&A*, **609**, A129
- Colzi, L., Sipilä, O., Roueff, E., Caselli, P., & Fontani, F. 2020, *A&A*, **640**, A51
- Dislaire, V., Hily-Blant, P., Faure, A., et al. 2012, *A&A* **537**, A20
- Endres, C. P., Schlemmer, S., Schilke, P., Stutzki, J., & Müller, H. S. P. 2016, *J. Mol. Spec.*, **327**, 95
- Fontani, F., Pascucci, I., Caselli, P., et al. 2007, *A&A*, **470**, 639
- Fontani, F., Palau, A., Caselli, P., et al. 2011, *A&A*, **529**, L7
- Fontani, F., Busquet, G., Palau, A., et al. 2015a, *A&A*, **575**, A87
- Fontani, F., Caselli, P., Palau, A., Bizzocchi, L., & Ceccarelli, C., 2015b, *ApJ*, **808**, 46
- Fontani, F., Ceccarelli, C., Favre, C., et al. 2017, *A&A*, **605**, A57
- Fontani, F., Vagnoli, A., Padovani, M., et al. 2018, *MNRAS*, **481**, L79
- Foster, J. B., Jackson, J. M., Barnes, P. J., et al. 2011, *ApJS*, **197**, 25
- Hily-Blant, P., Walmsley, C. M., Pineau Des Forêts, G., & Flower, D. 2010, *A&A*, **513**, A41
- Hily-Blant, P., Bonal, L., Faure, A., & Quirico, E. 2013, *Icarus*, **223**, 582
- Lichtenberg, T., Golabek, G. J., Burn, R., et al. 2019, *Nat. Astron.*, **3**, 307
- Ligterink, N. F. W., El-Abd, S. J., Brogan, C. L., et al. 2020, *ApJ*, **901**, L37
- Loison, J.-C., Wakelam, V., & Hickson, K. M. 2014, *MNRAS*, **443**, L398
- López-Sepulcre, A., Kama, M., Ceccarelli, C., 2013, *A&A*, **549**, L114
- Mininni, C., Beltrán, M. T., Rivilla, V. M., et al. 2020, *A&A*, **644**, A84
- Mininni, C., Fontani, F., Sánchez-Monge, Á., et al. 2021, *A&A*, submitted
- Motte, F., Bontemps, S., & Louvet, F. 2018, *ARA&A*, **56**, 41
- Nkem, C., Hammami, K., Halalaw, I. Y., Owono Owono, L. C., & Jaidane, N.-E. 2014, *A&SS*, **349**, 171
- Padoan, P., Pan, L., Juvella, M., Haugbølle, T., & Nordlund, A. 2020, *ApJ*, **900**, 82
- Padovani, M., Galli, D., & Glassgold, A. E. 2009, *A&A*, **501**, 619
- Pudritz, R. E. 2002, *Science* **295**, 68
- Quénard, D., Vastel, C., Ceccarelli, C., et al. 2017, *MNRAS*, **470**, 3194
- Rivilla, V. M., Jiménez-Serra, I., Martín-Pintado, J., & Sanz-Forcada, J. 2014, *MNRAS*, **437**, 1561
- Rivilla, V. M., Drozdovskaya, M. N., Altwegg, K., et al. 2020, *MNRAS*, **492**, 1180
- Semenov, D., Hersant, F., Wakelam, V., et al. 2010, *A&A*, **522**, A42
- Schilke P., Walmsley, C. M., Henkel, C., & Millar, T. J., 1991, *A&A*, **247**, 487
- Semaniak, J., Minaev, B. F., Derkach, A. M., et al. 2001, *ApJS*, **135**, 275
- Sipilä, O., Caselli, P., Redaelli, E., Juvella, M., & Bizzocchi, L. 2019a, *MNRAS*, **487**, 1269
- Sipilä, O., Caselli, P., & Harju, J. 2019b, *A&A*, **631**, A63
- Tan, J. C., Beltrán, M. T., Caselli, P., et al. 2014, *Protostars and Planets VI*, eds. H. Beuther, R. S. Klessen, C. P. Dullemond, & Th. Henning (Tucson: University of Arizona Press), 149
- Todd, Z. R., & Öberg, K. I. 2020, *Astrobiology*, **20**, 1109
- Vasyunina, T., Vasyunin, A. I., Herbst, et al. 2014, *ApJ*, **780**, 85
- Wakelam, V., Loison, J.-C., Herbst, E., et al. 2015, *ApJS*, **2017**, 20
- Woon, D. E., & Herbst, E. 2009, *ApJS*, **185**, 273
- Yan, Y. T., Zhang, J. S., Henkel, C., et al. 2019, *ApJ*, **877**, 154
- Zapata, L. A., Ho, P. T. P., Fernández-López, M., et al. 2020, *ApJ*, **902**, L47
- Ziurys, L. M., & Turner, B. E. 1986, *ApJ*, **302**, L31

Appendix A: Model predictions for different ζ

We show in this appendix the predictions of our chemical models for values of ζ that are different from the canonical value $\zeta = 1.3 \times 10^{-17} \text{ s}^{-1}$ adopted in Fig. 7.

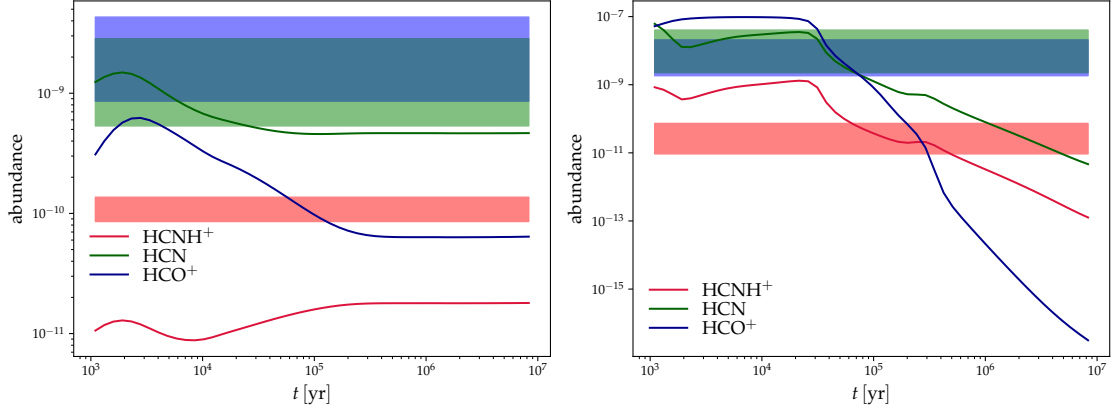


Fig. A.1. Same as Fig. 7, but assuming a cosmic-ray ionisation rate $\zeta = 1.3 \times 10^{-14} \text{ s}^{-1}$.

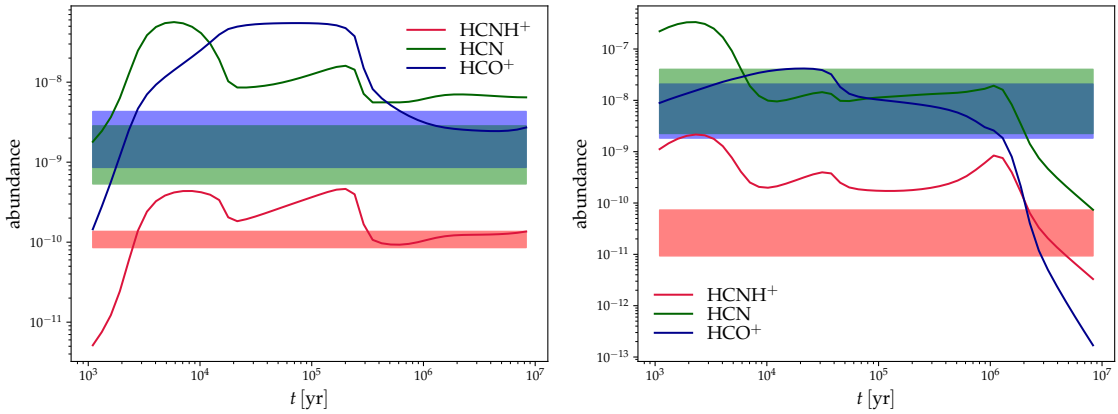


Fig. A.2. Same as Fig. A.1, but for $\zeta = 1.3 \times 10^{-15} \text{ s}^{-1}$.

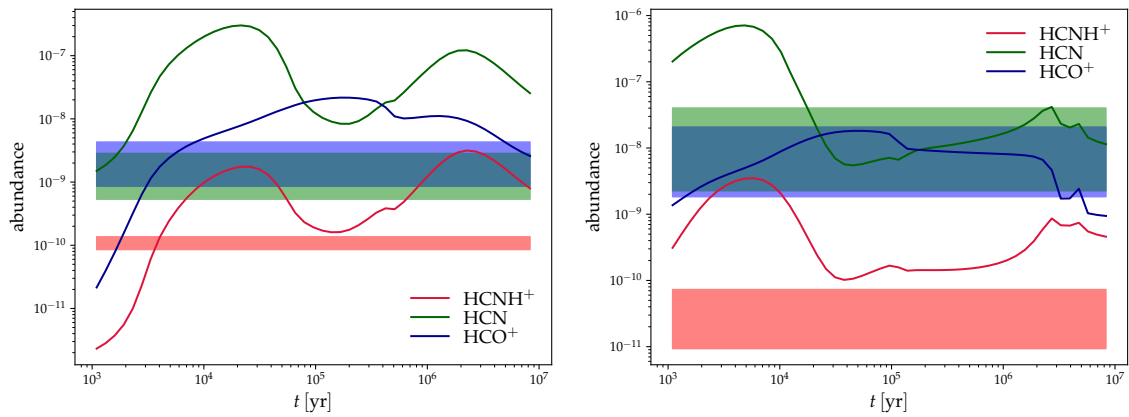


Fig. A.3. Same as Fig. A.1, but for $\zeta = 1.3 \times 10^{-16} \text{ s}^{-1}$.